





Promoting ethylene production over a wide potential window on Cu crystallites induced and stabilized via current shock and charge delocalization

Hao Sun^{1,2,5}, Ling Chen ^{3,5}, Likun Xiong^{1,2}, Kun Feng⁴, Yufeng Chen⁴, Xiang Zhang^{1,2}, Xuzhou Yuan^{1,2}, Baiyu Yang^{1,2}, Zhao Deng ^{1,2}, Yu Liu^{1,2}, Mark H. Rummeli^{1,2}, Jun Zhong^{4✉}, Yan Jiao ^{3✉} & Yang Peng ^{1,2✉}

Electrochemical CO₂ reduction (CO₂RR) in a product-orientated and energy-efficient manner relies on rational catalyst design guided by mechanistic understandings. In this study, the effect of conducting support on the CO₂RR behaviors of semi-conductive metal-organic framework (MOF) — Cu₃(HITP)₂ are carefully investigated. Compared to the stand-alone MOF, adding Ketjen Black greatly promotes C₂H₄ production with a stabilized Faradaic efficiency between 60-70% in a wide potential range and prolonged period. Multicrystalline Cu nano-crystallites in the reconstructed MOF are induced and stabilized by the conducting support via current shock and charge delocalization, which is analogous to the mechanism of dendrite prevention through conductive scaffolds in metal ion batteries. Density functional theory calculations elucidate that the contained multi-facets and rich grain boundaries promote C-C coupling while suppressing HER. This study underlines the key role of substrate-catalyst interaction, and the regulation of Cu crystalline states via conditioning the charge transport, in steering the CO₂RR pathway.

¹ Soochow Institute for Energy and Materials Innovations, College of Energy, Soochow University, 215006 Suzhou, P. R. China. ² Key Laboratory of Advanced Carbon Materials and Wearable Energy Technologies of Jiangsu Province, Suzhou, P. R. China. ³ School of Chemical Engineering and Advanced Materials, The University of Adelaide, Adelaide, SA 5005, Australia. ⁴ Institute of Functional Nano & Soft Materials (FUNSOM), Jiangsu Key Laboratory for Carbon-Based Functional Materials & Devices, Soochow University, 215123 Suzhou, China. ⁵ These authors contributed equally: Hao Sun, Ling Chen.

✉email: jzhong@suda.edu.cn; yan.jiao@adelaide.edu.au; ypeng@suda.edu.cn

The escalating climate change originating from the greenhouse effect due to excessive CO₂ emission urges the mankind to realize carbon neutrality as early as possible^{1,2}. Among the multiple strategic route maps, electrocatalytic reduction of carbon dioxide (CO₂RR) driven by renewable energy is especially tempting, as it simultaneously addresses both the environmental and resource crises^{3,4}. Copper in various forms have been demonstrated highly potent in catalyzing CO₂ conversion into a diversity of hydrocarbons and oxygenates, owing to its modest binding to many of the key CO₂RR intermediates^{5,6}. This, however, also leads to the lack of product selectivity in Cu-catalyzed CO₂RR as a result of the scaling relation among those intermediate binding^{7,8}. To take advantage of the product diversity while maximizing the selectivity of individual target, many structural mutations of Cu have been explored, including morphology and facet control^{9,10}, creation of grain boundaries^{11,12}, under-coordinated sites^{13,14}, and mixed valence states^{15,16}, as well as surface functionalization and segregation^{17,18}. Nonetheless, energy efficiency and product selectivity, especially on those value-added multiple-carbon products, remain as the major hurdles for ultimately deploying the technology in a technoeconomic fashion.

Previous studies showed that the substrates for catalyst loading, in most cases the carbon support, play a critical role in steering the CO₂RR pathway and stabilizing the catalytic process^{19,20}. For instance, Strasser and colleagues²¹ showed that the dispersion of Cu₂O nanocubes on a carbon support sharply shifted the selectivity pattern toward C₁, whereas its unsupported counterpart achieved a sustained C₂₊ Faradaic efficiency (FE). In situ formation of small Cu seeds with larger interparticle distance were attributed to the witnessed C₁ selectivity on the supported Cu₂O. Differently, Hwang and colleagues showed that Cu₂O nanoparticles immobilized on a carbon support via cysteamine doubled the FE of C₂H₄ in comparison to the unsupported catalyst and ascribed this selectivity enhancement to the electrochemical fragmentation of Cu₂O nanoparticles into compactly stacked smaller particles that are more liable to oxidation²². In another study, by pre-reducing the Cu nodes in a conductive metal organic framework (MOF) (CuHHTP) into Cu₂O quantum dots, Cao and co-workers achieved a high selectivity of CH₄ formation, which was attributed to ample hydrogen bonding from the substrate in stabilizing key intermediates²³. Thus, it is vitally important to assess the effect of carbon support on CO₂RR and scrutinize the substrate–catalyst interaction, as well as the charge transport behavior, for a better mechanistic understanding.

MOFs have been perceived as a unique category of CO₂RR catalyst since they offer a tunable platform to systematically alter the metal site coordination²⁴, regulate CO₂ and electrolyte counterions in the Helmholtz layer²⁵, and control over the intermediate binding²⁶. However, the stability of MOFs during the electrolytic process has been always a limiting issue, so that their electrochemical reconstruction (which is almost unavoidable, especially under high current conditions) to derive more robust catalyst ensembles is gaining increasing attentions^{27,28}. Consequently, when the controllable electrochemical reconstruction of MOFs is the subject of study, their chemical stability in the electrolyte is a premise²⁹. For that, in the current study we set to investigate the CO₂RR behaviors of a semi-conductive MOF—Cu₃(HITP)₂ (HITP = 2,3,6,7,10,11-hexamino-triphenylene) with and without adding the conducting support of Ketjen Black (KB). Cu₃(HITP)₂ was synthesized in an alkaline environment and thus, unlike many carboxylic MOFs, was born chemically resilient to the common electrolytes of CO₂RR. This should endow a unique opportunity to allow us to focus on their electrochemical reconstruction and catalyst–support interaction during the electrochemical process (Fig. 1a). We found that

adding KB enabled greatly promoting the C₂H₄ production with stabilized FE between 60 and 70% in a wide potential range and prolonged testing period, whereas the stand-alone MOF yielded more mixed reduction products. Operando X-ray absorption spectroscopy (XAS), serial post-reaction X-ray diffraction (XRD), and transmission electron microscope (TEM) analyses in conjunction with density functional theory (DFT) calculations were further carried out to correlate the product selectivity with structural characteristics of the reduced Cu moieties, furnishing fresh insights into the substrate–catalyst interaction and promoted C–C coupling on multicrystalline Cu nano-crystallites.

Results

Structural characterization of Cu₃(HITP)₂. Cu₃(HITP)₂ with high crystallinity was synthesized following the method developed by Dincă and co-workers recently³⁰. TEM taken on Cu₃(HITP)₂ revealed rod-like crystals of 30–40 nm in diameter (Fig. 1b), while energy-dispersive X-ray elemental mapping by high-angle annular dark-field scanning TEM confirmed the homogeneous elemental distribution of Cu, N, and C (Supplementary Fig. 1). Owing to the in-plane electron delocalization and through-space charge transport³¹, Cu₃(HITP)₂ demonstrated a semi-conductivity of 0.14 S cm⁻¹ (Fig. 1c), as measured at room temperature by the four-point probe method and in line with the previous reported values³¹. The XRD pattern in Fig. 1d exhibiting prominent diffraction peaks between 3° and 30° well matched that previously reported for Cu₃(HITP)₂^{30–32}, affirming the successful synthesis of the MOF structure with high crystallinity. X-ray photoelectron spectroscopy of Cu 2p_{3/2} exhibited a mixture of Cu²⁺ (933.5 eV) and Cu⁺ (931.8 eV) states in Cu₃(HITP)₂ (Supplementary Fig. 2)³¹, which was further corroborated by the X-ray absorption near edge structure (XANES, Supplementary Fig. 3). While the main peak at 398.5 eV in the N 1s spectrum was attributed to the Cu–N motif (Supplementary Fig. 4)³¹, the shoulder at 396.7 eV corresponded to the decrease in the N valence caused by the uncoordinated amines at the edge or defect sites of Cu₃(HITP)₂³³.

CO₂RR of Cu₃(HITP)₂ with or without KB. Considering the alkaline stability and intrinsic conductivity of Cu₃(HITP)₂, electrochemical CO₂RR performance was evaluated without or with adding KB as the conducting agent in CO₂-saturated KHCO₃ electrolyte. Correspondingly, the catalysts were denoted as Cu₃(HITP)₂ and KB@Cu₃(HITP)₂, respectively. First of all, linear sweep voltammeteries (LSVs, with a rate of 50 mV s⁻¹) taken on KB@Cu₃(HITP)₂ showed notably higher current densities than those of Cu₃(HITP)₂ in both N₂- and CO₂-purged electrolytes (Supplementary Fig. 5), indicating the addition of KB helped to promote the Faradaic processes including both hydrogen evolution reaction (HER) and CO₂RR. In addition, both KB@Cu₃(HITP)₂ and Cu₃(HITP)₂ gave higher current densities under CO₂RR conditions, affirming that the Cu-containing MOF was effective in catalyzing electrochemical CO₂ reduction. When normalized to the electrochemically active surface area estimated by measuring the double-layer capacitance (C_{dl}), the LSV current densities of KB@Cu₃(HITP)₂ were still higher than those of Cu₃(HITP)₂ (Supplementary Fig. 6), suggesting the intrinsic higher catalytic activity of the former.

On analyzing the reduction products, it was impressive to see KB@Cu₃(HITP)₂ exhibiting a higher and more stable C₂H₄ selectivity and yield (Fig. 2a, b and Supplementary Fig. 7). For KB@Cu₃(HITP)₂, the production of C₂H₄ started at -0.85 V (reversible hydrogen electrode (RHE), hereafter all the potential mentioned are referenced to this format) and reached a maximum FE of 70% at -1.37 V with concomitantly decreased

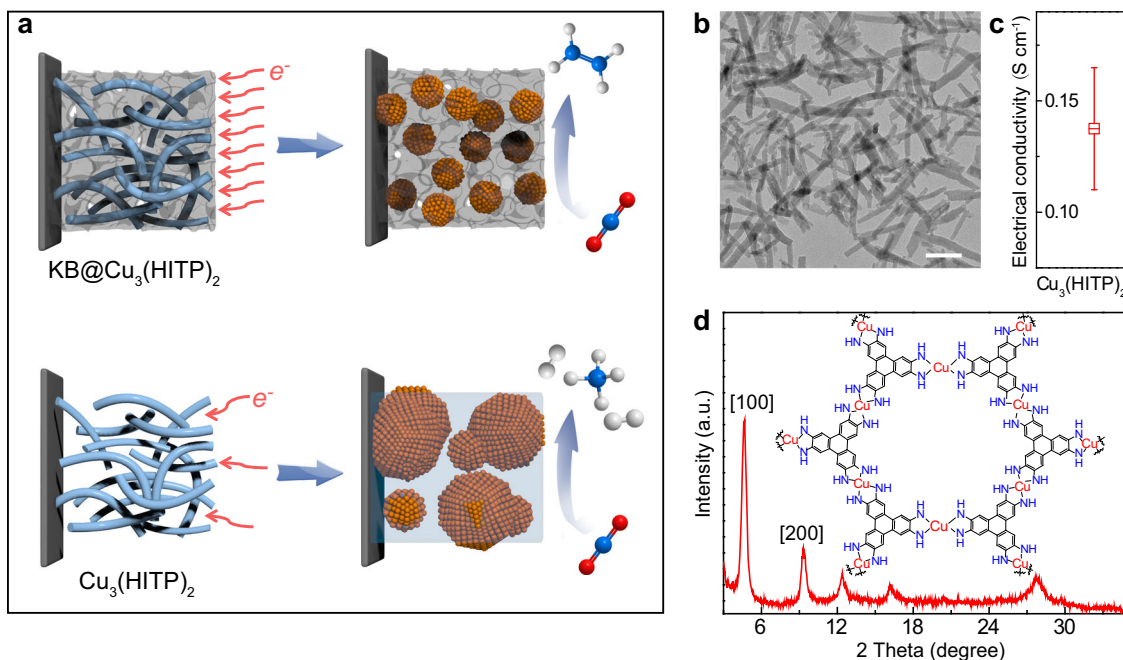


Fig. 1 Schematic representation and structure characterization. **a** Schematic diagrams showing the modulation of CO₂RR product selectivity by Cu₃(HITP)₂-derived Cu⁰ entities in the presence (top) or absence (bottom) of carbon support. **b** TEM image, **c** electrical conductivity measured by the four-probe method, and **d** XRD pattern of the as-synthesized Cu₃(HITP)₂. The scale bar in **b** is 200 nm. Error bars represent the standard deviation of three independent measurements.

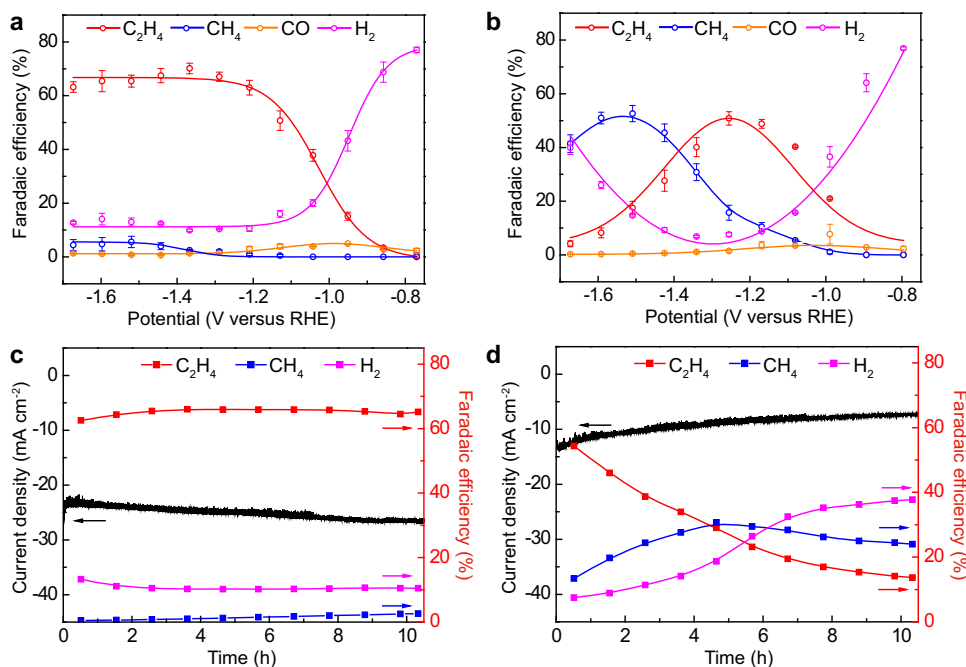


Fig. 2 Electrochemical CO₂RR performances. FEs of C₂H₄, CH₄, CO, and H₂ on **a** KB@Cu₃(HITP)₂ and **b** Cu₃(HITP)₂. The 10-h chronoamperometric test at -1.25 V for **c** KB@Cu₃(HITP)₂ and **d** Cu₃(HITP)₂ showing the evolution of total current density and FEs of C₂H₄, CH₄, and H₂. Error bars represent the standard deviation of three independent measurements.

H₂ yield (Fig. 2a). Of note, the FEs of C₂H₄ maintained over 63% within the wide potential range from -1.20 to -1.67 V, whereas those of CH₄ and CO were trivial during the entire CO₂RR test. In comparison, the FEs of C₂H₄ for Cu₃(HITP)₂ displayed a maximum of 51% at -1.25 V and thereafter decreased continuously (Fig. 2b). Meanwhile, a notable CH₄ production was observed attaining its maximum FE of 53% at -1.51 V,

accompanied by a continuous increase in H₂ yield (Fig. 2b). The different CO₂RR behaviors between KB@Cu₃(HITP)₂ and Cu₃(HITP)₂, especially on the varied C₂H₄ and CH₄ production, implied a different structural mutation of the Cu₃(HITP)₂ MOF during CO₂RR, which will be closely inspected later.

In addition to the C₂H₄ FE of >60% in a wide potential range, KB@Cu₃(HITP)₂ also demonstrated a high partial current density

reaching 37.4 mA cm^{-2} at -1.67 V (Supplementary Fig. 7), which is seldom seen in H cells (Supplementary Table 1). Moreover, at the applied potential of -1.25 V , $\text{KB@Cu}_3(\text{HITP})_2$ showed a good CO_2RR stability, with the total current density increased slightly from 23.3 to 26.3 mA cm^{-2} and C_2H_4 FE constantly above 64% for a duration of 10 h (Fig. 2c). By contrast, in the same testing period the C_2H_4 FE of $\text{Cu}_3(\text{HITP})_2$ decreased continuously from 52 to 13% , concomitant with a drop of total current density from 13.3 to 7.2 mA cm^{-2} (Fig. 2d). As for CH_4 production, it was intriguing to see both its FE and partial current density on $\text{Cu}_3(\text{HITP})_2$ were higher than those on $\text{KB@Cu}_3(\text{HITP})_2$, suggesting that the former was less competent in triggering C-C coupling. The liquid reduction products, analyzed by nuclear magnetic resonance (NMR), were also collected for both $\text{KB@Cu}_3(\text{HITP})_2$ and $\text{Cu}_3(\text{HITP})_2$, revealing a mixture of formate, ethanol, and propanol with a total FE $< 30\%$ at all potentials (Supplementary Fig. 8). Thus, our focus of this study will be mainly placed on comparing the main gaseous products.

Operando XAS on the Cu states. To track the change of Cu states for $\text{KB@Cu}_3(\text{HITP})_2$ and $\text{Cu}_3(\text{HITP})_2$ during CO_2RR and elucidate the origin of their catalytic difference, both potential- and time-dependent operando XAS were carried out by looking into the Cu K-edges. For $\text{KB@Cu}_3(\text{HITP})_2$ (Fig. 3a), upon the application of a negative potential at -0.86 V , the positive $\text{Cu}^{\delta+}$ ($1 < \delta < 2$) state of the MOF turned into Cu^0 , showing consistent pre-edge and white-line features (marked A, B, C in the XANES spectra of Fig. 3a) to those of Cu foil. In stark contrast, $\text{Cu}_3(\text{HITP})_2$ showed a more gradual change of Cu states as the applied potential decreased from -0.86 to -1.37 V (Fig. 3b). While the pre-edge and white-line peaks common to Cu^{2+} in

CuO and $\text{Cu}_3(\text{HITP})_2$ (marked as D and E in Fig. 3b) were still retained at -1.42 V , those of Cu^0 also started to evolve at the applied potential of -1.08 V , especially for the absorption edge at 8981 eV (feature A, due to the $1s \rightarrow 4p_z$ transition)³⁴. Clearly, these observations indicated that the $\text{Cu}^{\delta+}$ state in $\text{KB@Cu}_3(\text{HITP})_2$ was more readily reduced than that in $\text{Cu}_3(\text{HITP})_2$, likely due to the high current density from KB addition.

Similarly, the time-dependent XANES spectra of $\text{KB@Cu}_3(\text{HITP})_2$ collected at a constant potential of -1.25 V showed the $\text{Cu}^{\delta+}$ state in $\text{KB@Cu}_3(\text{HITP})_2$ was reduced to Cu^0 within only 8 min (Fig. 3c), whereas that in $\text{Cu}_3(\text{HITP})_2$ took 72 min to match the XANES spectrum of Cu foil (Fig. 3d). Furthermore, the serial Fourier-transform extended XAFS (FT-EXAFS) spectra of $\text{KB@Cu}_3(\text{HITP})_2$ showed a rapid evolution of the metallic Cu-Cu bond at 2.2 \AA and the disappearance of the MOF-related Cu-N peak at 1.5 \AA within 8 min (Fig. 3e), corroborating that the $\text{Cu}^{\delta+}$ nodes in the MOF were quickly and fully reduced. In the next hour, the intensity of the Cu-Cu coordination peak did not change much, indicating that the as-formed Cu^0 moieties remained mostly stable. On the other hand, the sequential FT-EXAFS spectra of $\text{Cu}_3(\text{HITP})_2$ displayed a gradual decay of the Cu-N coordination but intensification of the Cu-Cu peak within the whole testing period of 72 min (Fig. 3f), attesting to slower change of the MOF structure with gradually reduced Cu states. Taken together from the above electrochemical and XAS studies, it becomes evident that a high current shock endowed by adding the more conductive KB enables to quickly reduce the Cu nodes in the semi-conductive MOF of $\text{Cu}_3(\text{HITP})_2$.

Ex situ time-lapse XRD and TEM. Ex situ time-lapse XRD and TEM were used to track the structural changes of $\text{KB@Cu}_3(\text{HITP})_2$ and $\text{Cu}_3(\text{HITP})_2$ under a fixed CO_2RR potential of -1.25 V . As

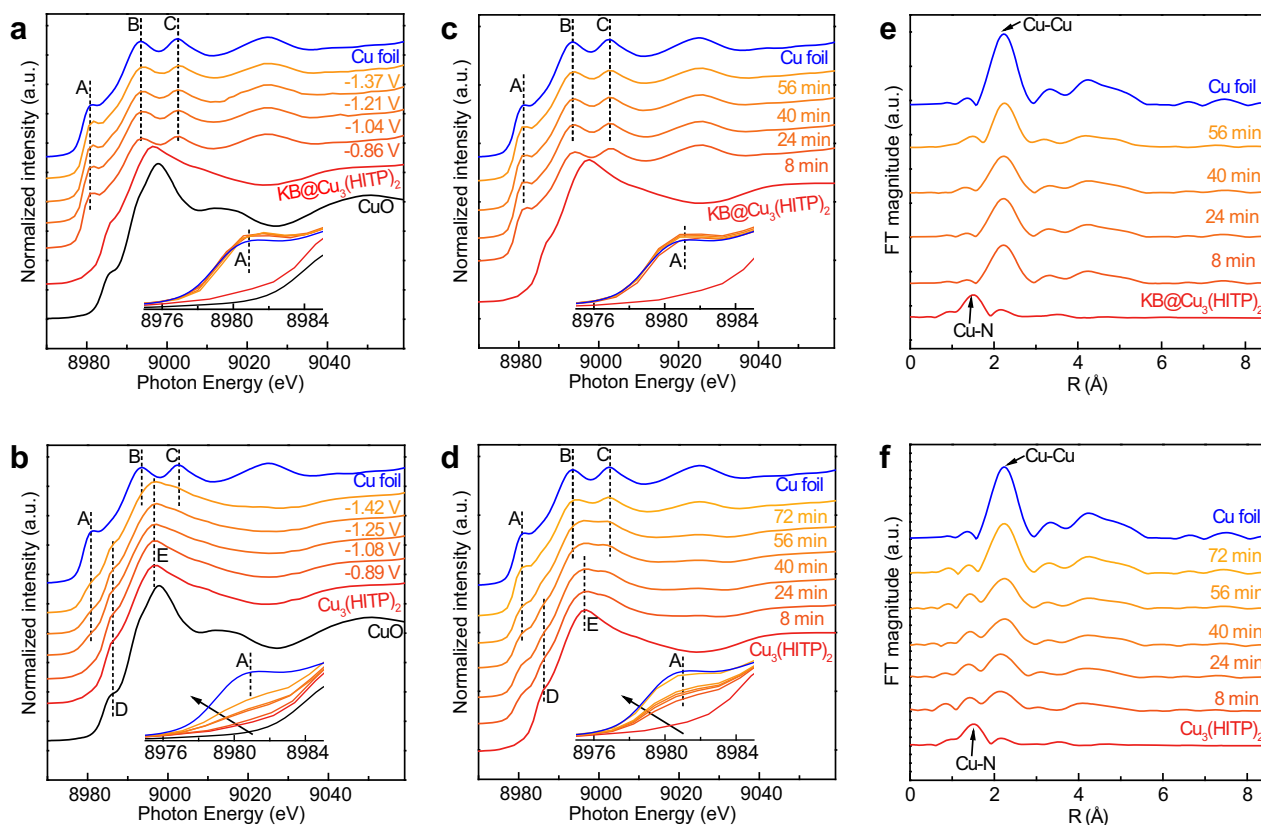


Fig. 3 Operando XAS. Operando Cu K-edge XAS of **a** $\text{KB@Cu}_3(\text{HITP})_2$ and **b** $\text{Cu}_3(\text{HITP})_2$ at different potentials during CO_2RR . Operando Cu K-edge XAS of **c** $\text{KB@Cu}_3(\text{HITP})_2$ and **d** $\text{Cu}_3(\text{HITP})_2$ as a function of reaction time at -1.25 V . The corresponding time-dependent FT-EXAFS for **e** $\text{KB@Cu}_3(\text{HITP})_2$ and **f** $\text{Cu}_3(\text{HITP})_2$.

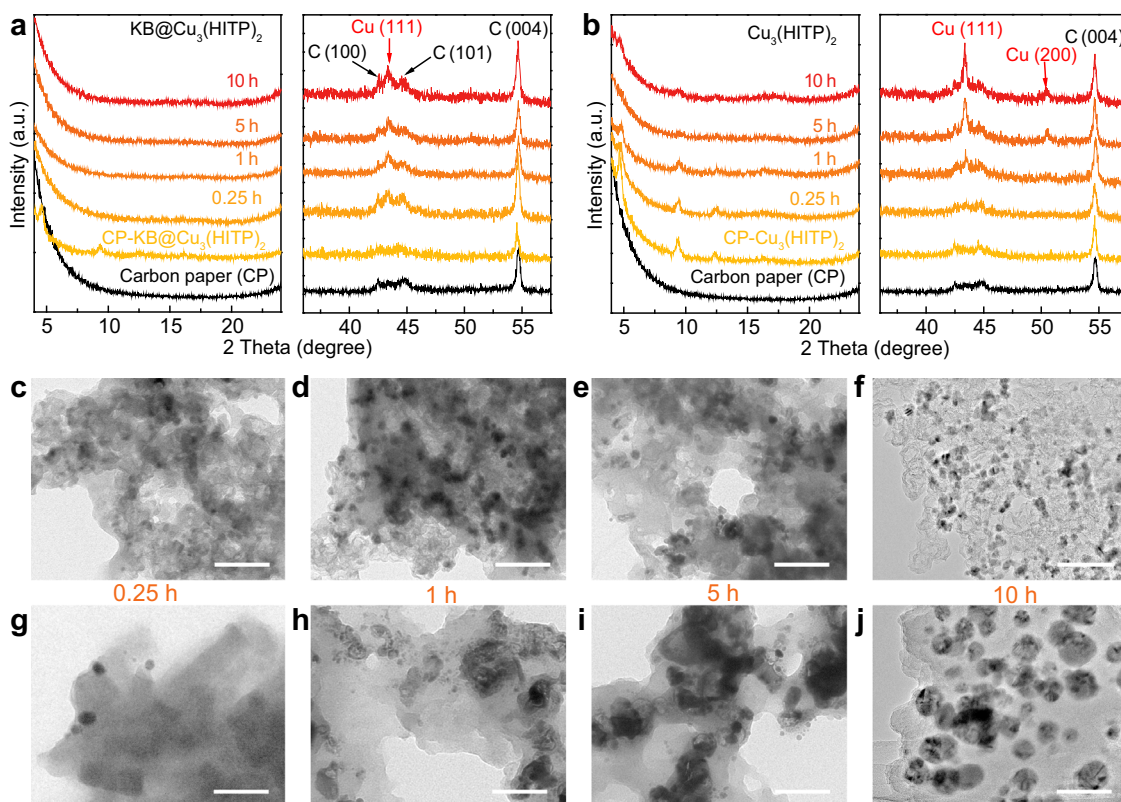


Fig. 4 Ex situ time-lapse XRD and TEM. Sequential XRD patterns of **a** KB@Cu₃(HITP)₂ and **b** Cu₃(HITP)₂ at -1.25 V. TEM images taken on **c-f** KB@Cu₃(HITP)₂ and **g-j** Cu₃(HITP)₂ after a chronoamperometric testing period of 0.25, 1, 5, and 10 h at -1.25 V, respectively. The scale bars in **c-j** are 100 nm.

shown in the left panel of Fig. 4a, for KB@Cu₃(HITP)₂ the characteristic XRD peaks of the MOF disappeared completely after just 0.25 h of testing. In the meantime, a Cu(111) peak at 43.3° can be distinguished sandwiched between the C(100) and C(101) diffractions, and its intensity changed only marginally in the next 10 h (Fig. 4a, right panel). This observation is in good agreement with the previous XAS results, corroborating the quick reduction of Cu^{δ+} centers in the reticular network of the MOF to form metallic Cu species. By contrast, for the stand-alone Cu₃(HITP)₂, diffraction peaks specific to the MOF were still distinguishable after even a reaction period of 10 h (Fig. 4b, left panel), indicating that not all the catalyst was decomposed. Different from that of KB@Cu₃(HITP)₂, the intensity of the Cu(111) peak observed on Cu₃(HITP)₂ grew continuously along the reaction time, together with the gradual emergence of a Cu(200) peak at 50.4° (Fig. 4b, right panel). Again, the different trend of XRD evolution observed above on KB@Cu₃(HITP)₂ and Cu₃(HITP)₂ suggested that in the former the metallic Cu species were quickly formed and remained relatively stable, whereas in the latter Cu^{δ+} were reduced more gradually but aggregated into larger Cu particles of higher crystallinity (according to the Debye-Scherrer rule, Supplementary Fig. 9 and Table 2)³⁵, which will be further examined by the following TEM studies.

Figure 4c-f, g-j displayed the TEM images taken on KB@Cu₃(HITP)₂ and Cu₃(HITP)₂ after a chronoamperometric testing period of 0.25, 1, 5, and 10 h at -1.25 V, respectively. The nano-rod morphology of the as-prepared Cu₃(HITP)₂ was absent in all post-electrolytic KB@Cu₃(HITP)₂ and Cu₃(HITP)₂ samples, indicating the corruption of the MOF topologic structure. Particularly, for KB@Cu₃(HITP)₂, Cu nanoparticles of 10 ± 2 nm were visible after 0.25 h, and beyond that the particle size remained mostly unchanged (Fig. 4c-f). As summarized in Supplementary Fig. 10a, the insignificant change of Cu particle

size observed here coincided well with the stable C₂H₄ production seen in Fig. 2c. In contrast, for Cu₃(HITP)₂, the average size of Cu particles reduced out from the MOF increased from 11 ± 3 nm at 0.25 h to 39 ± 8 nm after 10 h (Fig. 4g-j), consistent with the above XRD observations (Fig. 4b and Supplementary Table 2). Correspondingly, the FE of C₂H₄ was reduced from the initial 52 to 13%, while that of H₂ increased from 7.5 to 37% (Fig. 2d). This suggests that the growth of Cu particle size correlates to the decrease in C₂H₄ production and increase in H₂ yield (Supplementary Fig. 10b). Similar evolution of Cu particles was also observed in the serial potential-dependent TEM images (Supplementary Fig. 11), showing the severe aggregation of Cu particles in Cu₃(HITP)₂ and mostly unchanged Cu particle size in KB@Cu₃(HITP)₂ while ramping down the potential from -1.21 to -1.75 V. Here, once again, the large Cu particle size in Cu₃(HITP)₂ correlated to the increase in H₂ FE and decrease in C₂H₄ FE (Supplementary Fig. 12).

Collectively from the above observations, two facts about the CO₂RR processes on KB@Cu₃(HITP)₂ and Cu₃(HITP)₂ become clear. First, the addition of KB caused the quick reduction of Cu^{δ+} nodes from the MOF into small Cu⁰ crystallites and helped stabilize them thereafter. Without the conducting support, the metal nodes were reduced more slowly but easily aggregated. We attribute this phenomenon mainly to the high current density and homogenized charge distribution on the electrode endowed by the conducting support. This is indeed analogous to the process of dendrite formation that is often observed on the anodes of metal ion batteries, where improved charge delocalization on the less-conductive solid-electrolyte interface (SEI) would greatly suppress dendrite growth^{36,37}. Likewise, in the current case of Cu₃(HITP)₂ the gradually reduced Cu species tend to form aggregates due to inhomogeneous surface polarization and inadequate nuclei seeding,

whereas for KB@Cu₃(HITP)₂ the conducting substrate can afford better charge transport to effectively reduce the metal nodes and dissipate localized charges for mitigating Cu agglomeration. Second, smaller crystallites of Cu reduced out from the MOF were more beneficial for C₂H₄ production^{22,28}, whereas larger Cu particles tend to induce severe hydrogen evolution reaction. In between, a transition phase might be favorable for yielding CH₄.

Control studies with naked Cu nanoparticles. In order to see whether similar FE trends could also be observed for naked Cu nanocrystals when dispersed over a carbon support or whether it is related to the utilization of MOF precursors, we mixed commercial Cu nanoparticles (10–30 nm) with KB (denoted as KB@CuNPs) and tested their CO₂RR activity in H-cell. With the same mass loading, KB@CuNPs exhibited lower total current densities than those of KB@Cu₃(HITP)₂ at all applied potentials (Supplementary Fig. 13), indicative of inferior catalytic activity. The FEs of C₂H₄ for KB@CuNPs reached a maximum of 48% at –1.56 V (Supplementary Fig. 14a), which is lower than that of KB@Cu₃(HITP)₂ (~65%) at the same potential. At lower potentials, KB@CuNPs showed higher H₂ selectivity with FEs 3–4 times higher than those of KB@Cu₃(HITP)₂. In addition, the C₂H₄ selectivity of KB@CuNPs was unstable on the time scale, with the FE dropped from 47 to 11% within 8 h at the applied potential of –1.56 V (Supplementary Fig. 14b). Meanwhile, the FE of H₂ increased from 39 to 74%. Such differences in activity and selectivity between KB@Cu₃(HITP)₂ and KB@CuNPs underline the value of using MOF precursors to derive active Cu moieties toward enhanced CO₂RR performance. Based on this comparative study, we surmise that the crystalline structure of the MOF-derived Cu crystallites and their interaction with residual ligands both contribute to the observed performance enhancement. As part of the evidence, TEM images showed that the Cu nanoparticles in KB@CuNPs agglomerated into larger nanoparticles after 8 h of electrolysis (Supplementary Fig. 15), coinciding with the decrease in C₂H₄ and increase in H₂ selectivity. By contrast, the Cu crystallites in KB@Cu₃(HITP)₂ did not agglomerate over time, which implies the possible tethering effect of the residual ligands in addition to the effect of KB-promoted charge delocalization. The agglomeration of Cu nanoparticles on carbon paper after prolonged CO₂RR was also previously observed by Yang and colleagues³⁸. Above all, our control study with naked Cu nanoparticles underscores the unique advantage of MOF precursors to derive highly active Cu motifs upon reconstruction.

Mechanistic comprehension of the C₂H₄ selectivity on Cu nano-crystallites. To help further comprehend the observed structure–performance correlations from the aspect of atomic corrugations, we sought spherical aberration-corrected TEM (Cs-TEM) to dissect the lattice structure of the Cu nano-crystallites and nanoparticles derived from KB@Cu₃(HITP)₂ and Cu₃(HITP)₂, respectively, as well as DFT calculations to rationalize the associated C–C coupling process. Despite the much smaller particle size, Cu crystallites derived from KB@Cu₃(HITP)₂ after 10-h CO₂RR test exhibited rich facets and grain boundaries, as well as lattice defects, in TEM images. For instance, as shown in Fig. 5a and insets³⁹, various lattice planes of (111), (100), (220), etc. converged and were adjacent to each other, forming a highly complex lattice structure that are characteristic of pre-matured crystallites^{40,41}. The small Cu crystallites were then stacked upon one and another, dispersed in the amorphous carbon matrix containing evenly distributed N elements that were inherited from the MOF ligands (Supplementary Figs. 16 and 17). On the other hand, the lattice structure of Cu particles reduced from Cu₃(HITP)₂ was relatively dull, containing

less grain boundaries and defects. As shown in Fig. 5b and Supplementary Fig. 18, lattice fringes of the (111) plane with a *d*-spacing of 0.21 nm composed the main theme of the images, manifesting a more matured crystallinity. We attribute the observed difference in lattice diversity mainly to the relatively kinetics-driven Cu nucleation in KB@Cu₃(HITP)₂ but more of the thermodynamics-driven Cu growth in Cu₃(HITP)₂. That is to say, the as-formed Cu crystallites in KB@Cu₃(HITP)₂ were “frozen” in the earlier nucleation stage of crystal growth, where the packing of Cu atoms was more chaotic, leading to diverse lattice features⁴⁰. In contrast, the reduced Cu nuclei in Cu₃(HITP)₂, with less population, tend to grow into larger conglomerates exposing less lattice features owing to Ostwald ripening⁴¹.

Learning the highly diverse lattice features of Cu nanocrystallites from post-electrolytic KB@Cu₃(HITP)₂ and the relatively dull lattice structure of Cu particles reduced from Cu₃(HITP)₂, we now stand on a good position to construct atomic models for simulating the CO₂RR process. The difference in lattice configuration may result in non-identical electrochemical selectivity during CO₂RR as suggested by previous research⁴². Therefore, in the following DFT study we focus on the effect of lattice configuration on the selectivity for C₂ (e.g., ethylene) versus C₁ (e.g., methane) production.

The post-electrolytic KB@Cu₃(HITP)₂ sample was modeled by [101] Cu rectangular nanopyrramids (Cu-RNPs)⁴³ as shown in Supplementary Fig. 19. The single Cu-RNP model is based on a rectangular 5 × 5 × 1 Cu (101) surface; the four triangular sidewalls of the nanopyrramid are (100) and (111) facets at intervals. This model is in good agreement with Cs-TEM observation that (100) and (111) facets are converged and adjacent to each other (Fig. 5a). Moreover, the Cu-RNPs are in dense array with 5.1 Å between adjacent nanopyrramids, which represents the small Cu crystallites stacked and dispersed on the substrate (Supplementary Fig. 16). Meanwhile, the post-electrolytic Cu₃(HITP)₂ surface with a uniform lattice structure was represented by a 4 × 4 × 4 Cu(111) supercell (Supplementary Fig. 20).

Three active sites were identified on Cu-RNP that evenly distribute on the symmetrical sidewalls (Supplementary Fig. 21). We then carried out DFT calculations to acquire the full reaction pathway as proposed by Cheng et al.⁴⁴ toward main products observed in the experiment, including CH₄ and C₂H₄. The reaction pathways are summarized in Fig. 5c and Supplementary Figs. 22 and 23, with free energy for each reaction step given in Supplementary Tables 3 and 4. From these reaction pathways, further reduction of 2*CO on Cu-RNP proceeds in two major pathways, namely, (1) C₁ pathway (blue)—a conventional pathway toward CH₄ formation and (2) C₂ pathway which bifurcates from *CH₂–CHOH to C₂H₄ (green) and C₂H₅OH (orange). The direct hydrogenation after *CO adsorption (2*CO + H⁺ + e[–] → *CHO + *CO) has the highest endothermic energy in C₁ pathway, serving as the potential-determining step (PDS). PDS for the C₂ pathway is *CO dimerization and subsequent proton-coupled electron transfer (PCET) to *COH–CO (2*CO + H⁺ + e[–] → *COH–CO). We also found that the limiting potential for C₂ pathway on all active sites of Cu-RNP are significantly lower than those of C₁ pathway (–0.61 to –0.68 V vs –0.84 to –0.92 V), which indicates that CO₂RR can proceed preferentially toward C₂ with an inhibited CH₄ selectivity on Cu-RNP surface. In addition, for Cu-RNP C₂ pathway, the proceeding of 11th PCET to *CH₃–CHOH is endergonic with an uphill Δ*G* = 0.26 eV, in contrast to the exergonic protonation to *CH₂–CH (Δ*G* = –0.19 eV), suggesting a low C₂H₅OH selectivity on the surface. All these are consistent with the experimental observation that on KB@Cu₃(HITP)₂ the FE for C₂H₄ production

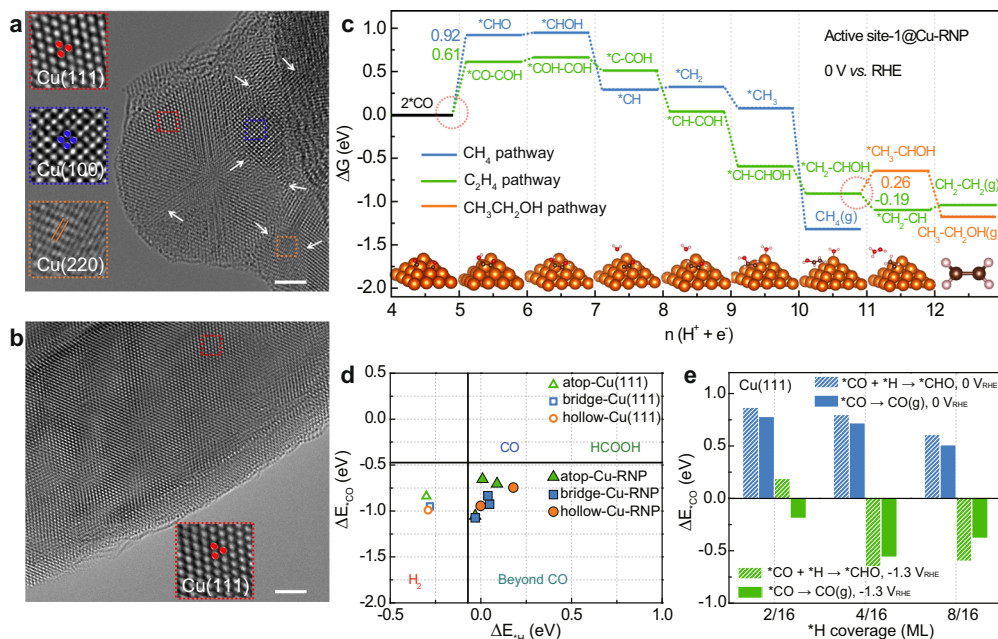


Fig. 5 CS-TEM images and DFT simulation. TEM images of **a** KB@Cu₃(HITP)₂ and **b** Cu₃(HITP)₂ after CO₂RR conducted at -1.25 V for 10 h in CO₂-saturated 0.1 M KHCO₃ electrolyte. **c** Reaction pathways starting with 2 *CO identified on active site-1 of [101] Cu rectangular nanopyramid (Cu-RNP) surface to model the post-electrolytic KB@Cu₃(HITP)₂ at 0 V. Insets are the atomic structures of intermediates along the C₂H₄ pathway. The key bifurcating points are highlighted with red circles and the unit of energy is eV. **d** Relation between ΔE_{CO} and ΔE_{H} at various sites on the Cu-RNP and Cu (111) surfaces. Vertical and horizontal black lines represent the equilibrium potential for $\text{H} \leftrightarrow \frac{1}{2} \text{H}_2$ and $\text{*CO} \leftrightarrow \text{CO}$, respectively and **e** the energetics of reactions $\text{*CO} + \text{*H} \rightarrow \text{*CHO}$ and $\text{*CO} \rightarrow \text{CO}$ (g) on the modeled post-electrolytic Cu₃(HITP)₂ surface of Cu (111) under various *H coverages and bias potentials. The scale bars in **a**, **b** are 2 nm.

is significantly higher than those of CH₄ and C₂H₅OH (Supplementary Fig. 8a).

The promoted C–C coupling and consequent high C₂H₄ selectivity on KB@Cu₃(HITP)₂ can be attributed to the enhanced *CO adsorption and geometric effect induced by rich grain boundaries and multi-facets on the reduced Cu nano-crystallites. As shown in Supplementary Fig. 24, the *CO binding on the boundary sites of Cu-RNP is significantly enhanced compared with those on basal sites and Cu(111). A strong *CO binding is highly sought after; for example, experimental efforts attribute the high C–C coupling activity to the strong *CO binding and the resulting high *CO coverage^{45,46}. More importantly, on Cu-RNP along the grain boundaries, the strong *CO adsorption site and the adjacent weak adsorption site coexist within an under-coordinated surface square area (Supplementary Fig. 21), which meets the *extended square principles* criteria toward a promoted C–C coupling⁴³. Consequently, the formation of *COH–CO on Cu-RNP is highly favored over that of *CHO and the C₂ pathway is thermodynamically more selective than C₁ pathway.

In addition to the promoted C–C coupling, the rich grain boundaries and multi-facets of Cu nano-crystallites on post-electrolytic KB@Cu₃(HITP)₂ can further contribute to higher C₂ selectivity by inhibiting competitive HER. We adopted the selectivity determining method proposed by Rossmeisl and colleagues⁶ to indicate product selectivity on the constructed models by *H and *CO binding energy. The results are summarized in Fig. 5e, which shows that all active sites from the Cu(111) surface (Supplementary Fig. 25a) fall in the HER dominant zone. In contrast, all active sites from the Cu-RNP surface (Supplementary Fig. 25b) fall in the CO₂RR dominant zone. The calculated selectivity on the two models is in good agreement with the experimental observation of stable C₂H₄ production with suppressed H₂ yield on KB@Cu₃(HITP)₂.

It is worth noting that on Cu₃(HITP)₂ the selectivity of C₂H₄ starts to decrease from -1.3 V with a continuous increase in H₂ and CH₄ (Fig. 2b). We attribute the decline of C₂H₄ to the *H site-blocking effects under negative potentials. It was reported that dominant *H can partially displace *CO under very negative potential, and the resultant low *CO coverage impedes the *CO dimerization, hence C₂H₄ production⁴⁴. We also observed that CH₄ production attained the maximum FE of 53% after -1.0 V vs RHE with negligible amount of CO (Fig. 2b). The main reason lies in that Cu₃(HITP)₂ exposes mainly Cu(111) facets (Fig. 5b), which are more selective toward CH₄ than CO under negative potentials according to previous experimental research^{47,48}. To reveal the origin of CH₄ selectivity over CO on Cu(111) surfaces, we simulated the key reaction step toward CH₄ formation: $\text{*CO} + \text{*H} \rightarrow \text{*CHO}$, and competing *CO desorption step: $\text{*CO} \rightarrow \text{CO}_{(\text{g})}$ on Cu(111) (Supplementary Fig. 26). During the simulation, different electrode potentials (0 and -1.3 V vs RHE) were considered by applying the constant electrode potential (CEP) method⁴⁹. At the same time, different surface *H coverages were considered (i.e., 2/16 ML, 4/16 ML and 8/16 ML), because previous experimental studies suggest that the coverage will increase to over 0.3 ML at high overpotential^{50,51}. We found that, on Cu(111) at 0 V vs RHE, both the *CHO formation and *CO desorption activities improve from low *H coverage (2/16 ML) through medium *H coverage (4/16 ML) to high *H coverage (8/16 ML), as shown in Fig. 5e. With bias potential of -1.3 V vs RHE, both reaction steps become exergonic, while the former reaction is more thermodynamically favorable with more negative energy changes (~ -0.64 vs -0.38 eV). The difference in energy change means that the reaction pathway proceeds toward CH₄ production at very negative potential via the *CHO formation, instead of CO release through *CO desorption. This conclusion is consistent with

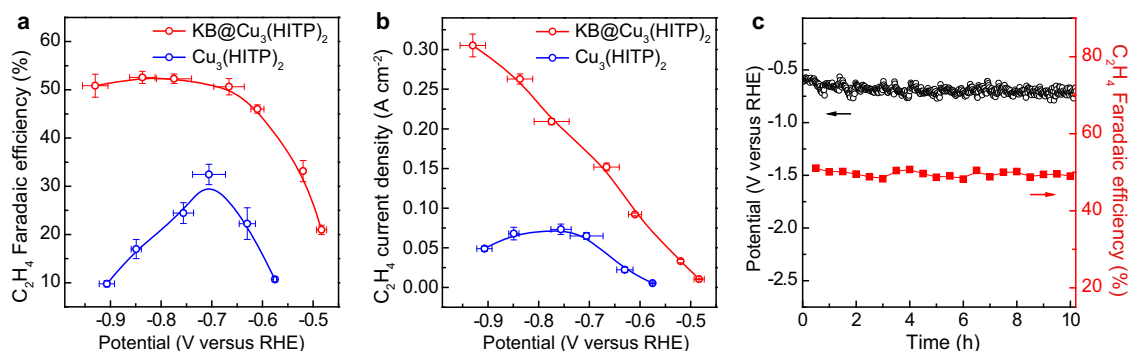


Fig. 6 Electrocatalytic CO₂RR performance in the flow cell. **a** FEs and **b** partial current densities of C₂H₄ at different potentials tested in the flow cell with 1 M KOH electrolyte for KB@Cu₃(HITP)₂ and Cu₃(HITP)₂. **c** Stability test of KB@Cu₃(HITP)₂ during 10 h of electrolysis under the current density of 300 mA cm⁻². Error bars represent the standard deviation of three independent measurements.

previous experimental research^{47,48}, as summarized in Supplementary Table 5.

Universality of the observations by extending to flow cell and Cu₃(HHTP)₂. As the CO₂RR kinetics are restricted by mass transportation in the H cell due to limited solubility of CO₂ in aqueous electrolytes⁵², flow-cell tests were further carried out in 1 M KOH to achieve high current densities (>100 mA cm⁻², Supplementary Fig. 27). For a better quantification of FEs, the chronopotentiometric mode was employed. Despite the different electrolyte from that utilized in H cell, KB@Cu₃(HITP)₂ still showed notably higher current densities than those of Cu₃(HITP)₂ (Supplementary Fig. 28). In addition, the onset potential of C₂H₄ production for KB@Cu₃(HITP)₂ was -0.48 V, which is earlier than that for Cu₃(HITP)₂ (-0.58 V). For KB@Cu₃(HITP)₂, the FE of C₂H₄ reached 51% at -0.67 V and stayed above it till -0.93 V (Fig. 6a), whereas that for Cu₃(HITP)₂ displayed a maximum of 32% at -0.71 V but thereafter gradually decreased to below 5% at -1.02 V (Fig. 6a and Supplementary Fig. 29). As for CH₄ production, the FE for KB@Cu₃(HITP)₂ was trivial and remained <9% during the entire CO₂RR test, while that for Cu₃(HITP)₂ continued to increase with decreasing potentials until a maximum of 53% at -0.85 V (Supplementary Fig. 29). Besides, the presence of KB inhibited HER, especially at more negative potentials. Consistently, KB@Cu₃(HITP)₂ exhibited higher C₂H₄ partial current densities than Cu₃(HITP)₂ did at all applied potentials and reached 305 mA cm⁻² at -0.93 V (Fig. 6b). KB@Cu₃(HITP)₂ also showed good electrocatalytic stability in the flow cell, which stably operated over 10 h at a current density of 300 mA cm⁻² (Fig. 6c). In general, the flow-cell tests on KB@Cu₃(HITP)₂ and Cu₃(HITP)₂, despite involving much higher current densities, showed similar trends of product selectivity to those in the H cell, corroborating the positive role of KB in promoting and stabilizing the C₂H₄ selectivity.

To testify the universality of the above phenomenon with respect to the KB effect on promoting and stabilizing ethylene production for semi-conductive Cu MOFs that are stable in alkaline conditions, we synthesized another similar MOF of Cu₃(HHTP)₂ (HHTP = 2,3,6,7,10,11-hexahydroxytriphenylene) by replacing the amine groups in HITP with hydroxyls (Supplementary Figs. 30 and 31). As expected, similar CO₂RR behaviors to that of Cu₃(HITP)₂ were also observed for Cu₃(HHTP)₂ (Supplementary Fig. 32). On KB@Cu₃(HHTP)₂, the FE of C₂H₄ was plateaued after -1.29 V (Supplementary Fig. 32a), coinciding with the stabilized Cu particle size at varying potentials from -1.22 to -1.65 V (Supplementary Fig. 33a–d). As for the stand-alone Cu₃(HHTP)₂, both the FEs of C₂H₄ and CH₄ increased first and then decreased, concomitant with the “V”-

shape voltage dependence of H₂ FEs (Supplementary Fig. 32b), which was also observed previously for Cu₃(HITP)₂ (Fig. 2b). Correspondingly, the serial TEM images taken on the post-electrolytic Cu₃(HHTP)₂ samples at different potentials showed the prominent growth of Cu particle size with increasing bias (Supplementary Fig. 33e–h). Thus, for both Cu₃(HITP)₂ and Cu₃(HHTP)₂, the addition of KB enables steering the CO₂RR pathway toward ethylene production by preserving the reduced Cu in their nano-crystallite state, which, as aforementioned, is induced and stabilized via high current shock and surface charge delocalization.

Discussion

CO₂RR behaviors of the semi-conductive MOF—Cu₃(HITP)₂—were studied with and without conducting support. It was found adding KB greatly promoted the C₂H₄ production with a stabilized FE between 60 and 70% in a wide potential range and prolonged test, whereas the stand-alone MOF produced more mixed reduction products during the reaction course. Operando XAS in conjunction with ex situ time-lapse XRD and TEM analyses clearly revealed that in the presence of KB tiny Cu crystallites were quickly reduced from the MOF and stabilized thereafter. By contrast, on Cu₃(HITP)₂ in the absence of KB, Cu nanoparticles were gradually reduced out and aggregated into larger sizes, which can be attributed to the poor surface charge delocalization, analogous to the process of dendrite growth at the SEI of metal ion batteries. By scrutinizing the detailed lattice structure using CS-TEM, a structural model comprising multifacets and grain boundaries was established via DFT to successfully rationalize the promoted C–C coupling on the Cu nano-crystallites derived from KB@Cu₃(HITP)₂. As a result, our study furnishes fresh insights into the steering of CO₂RR pathway by regulating and stabilizing Cu crystalline states via conditioning the charge transport on electrodes, which can be possibly extended to other metal–organic complexes.

Methods

Materials. Copper(II) sulfate pentahydrate (CuSO₄·5H₂O) was purchased from Sinopharm Chemical Reagent Co., Ltd. Triphenylene-2,3,6,7,10,11-hexaamine 6HCl (HATP·6HCl ≥98%) was provided by Shanghai Kaiyulin Co., Ltd. Triphenylene-2,3,6,7,10,11-hexaol (HHTP, ≥97%) was provided by Bide Pharmatech Ltd. Sodium acetate trihydrate (C₂H₃O₂Na·3H₂O, ≥99.5%) and cupric acetate anhydrous (Cu(C₂H₃O₂)₂) were obtained from Aladdin. Potassium bicarbonate (KHCO₃, ≥99.5%) were purchased from J&K Scientific Co., Ltd. *N,N*-dimethylmethanamide (DMF, ≥99.5%) and *N,N*-dimethylacetamide (DMA, ≥99.5%) were purchased from Greagent. Ethanol (C₂H₆O, ≥99.7%) was provided by Shanghai Lingfeng Chemical Reagent Co., LTD. The CO₂ gas (99.995%) was supplied by Suzhou Jinhong Gas Co. Ltd. All materials were used as received without further purification. The Cu NPs were purchased from Macklin. Deionized (DI) water was purified with a Sartorius arium mini ultrapure water system.

Synthesis of Cu₃(HITP)₂. In all, 7 mg (0.028 mmol) of CuSO₄·5H₂O was suspended in 3 mL of DMA and sonicated for 10 min. Then a solution of 10 mg (0.0186 mmol) of HATP·6HCl in 3 mL of water was added and sonicated for 10 min. A total of 4 mL of C₂H₃O₂Na aqueous solution (2 M) was then added at room temperature, and the mixture was heated in a 50 mL open glass vial with stirring for 2 h at 65 °C. The resulting black powder was filtered, washed with large amount of water and methanol, and dried under vacuum.

Synthesis of Cu₃(HHTP)₂. In all, 28.3 mg (0.156 mmol) of Cu(C₂H₃O₂)₂ and 14 mg (0.044 mmol) of HHTP was suspended in 3 mL of DI water and sonicated for 5 min. A total of 0.3 mL DMF was then added dropwise to this mixture followed by 5 min of sonication. The capped vial was heated at 80 °C for 6 h. The resulting blue powder was centrifuged, washed with large amount of water and ethanol, and dried under vacuum.

Characterizations. The crystalline phases of the products were analyzed by powder XRD measurements with a Bruker D8 Advance X-ray diffractometer using Cu-Kα radiation. One milligram of powder catalyst was loaded on 1 × 1 cm² of carbon paper for ex situ time-lapse XRD testing. The surface composition and valence states were analyzed with XPS, using an Escalab 250Xi X-ray photoelectron spectrometer (Thermo Fisher) with Al Kα (1486.6 eV) X-rays as the excitation source, and the binding energy of the C 1s peak at 284.8 eV was taken as an internal reference. The pass energy was 30 eV and the photoemission angle was 45°. The energy linearity detection was calibrated with Au 4f (83.96 eV), Ag 3d₅ (368.21), and Cu 2p (932.62 eV). The morphologies were examined by SEM conducted on a Hitachi SU8010 scanning electron microanalyzer with an accelerating voltage of 10 kV. The microstructures of the products were further characterized by TEM measured at 200 kV with a FEI TECNAI G20 field-emission TEM. Cs-TEM (FEI Titan Themis Cubed G2 300) was used to inspect atomic orientation of samples.

Electrochemical measurements. The CO₂ electro-reduction reactions were performed in a gas-tight, two-compartment H-cell controlled with an electrochemical workstation (CHI760E). Thereinto, the two compartments of H-cell are separated by an ion exchange membrane (Nafion perfluorinated membrane), and each compartment was filled with 40 mL of 0.1 M KHCO₃. A carbon rod was used as the counter electrode, and a calibrated Ag/AgCl electrode was used as the reference electrode. To prepare the catalyst ink for H-cell studies, 4 mg of the sample powder and 1 mg KB were mixed with 50 μL Nafion solution (5%) in 1 mL ethanol by ultrasonic dispersion for 15 min. Next, 10 μL of the as-prepared ink was drop-coated onto the glassy carbon electrode with a surface area of 0.197 cm². The working electrode was then dried at room temperature for subsequent testing. Before electrochemical measurements, a continuous CO₂ was purged into the cathodic compartment for at least 30 min. During the measurements, the CO₂ was bubbled into the electrolyte with a constant flow rate of 20 cm³ min⁻¹ controlled by a digital mass flow controller. The activation of the working electrode was carried out by repeatedly running cyclic voltammetry within the potential range from -0.5 to -1.8 V with a rate of 10 mV s⁻¹ for 20 min.

The flow cell comprises three chambers: gas, catholyte (gas diffusion electrode, YLS-30T), and anolyte (nickel foam, 0.8 mm thickness). The Ag/AgCl reference electrode was plugged in the center of catholyte chamber via a top drill hole. Catholyte and anolyte were separated by anion exchange membrane (Fumasep FAB-PK-130). Gas and catholyte were separated by the gas diffusion electrode. Using an electric airbrush, the catalyst dispersed in ethanol was spray-coated on the side of the gas diffusion electrode facing the electrolyte (0.8 mg cm⁻²), with the opposite side facing the gas chamber. Silicone gaskets with 2 × 0.5 cm² window were placed to assure adequate sealing of each chamber. The high-purity CO₂ was supplied to the gas chamber with a constant flow rate of 30 cm³ min⁻¹ monitored by a digital mass flow controller (Horiba). The flow-cell measurements were conducted in 1 M KOH with a constant flow rate of 20 mL min⁻¹ through a dual-channel peristaltic pump. The pH of 1 M KOH decreased slightly from 13.7 to 13.3 after 10 h of reaction (Supplementary Fig. 34). The cell resistances were measured via electrochemical impedance spectroscopy under open circuit, and 85% ohmic resistance correction was applied in all H-cell and flow-cell measurements.

The gas products were quantitatively analyzed using gas chromatography equipped with both flame ionization and thermal conductivity detectors (Agilent 7890B). The liquid products were collected after at least 5 h of electrolysis and quantitatively analyzed using 1H NMR spectroscopy with H₂O suppression. In all, 400 μL electrolyte mixed with 50 μL dimethyl sulfoxide (20 mM) and 100 μL D₂O was used as the internal standard. All the potentials were converted to RHE, according to the equation $E \text{ (vs RHE)} = E \text{ (vs Ag/AgCl)} + 0.059 \times \text{pH} + 0.198$.

Operando XAS measurements. The operando XAS spectra at the Cu K-edge were recorded at the BL11B beamline of Shanghai Synchrotron Radiation Facility. The electron storage ring operated at 3.5 GeV. The beam current of the storage ring was 220 mA in a top-up mode. The incident photons were monochromatized by a Si(111) double-crystal monochromator, with an energy resolution $\Delta E/E \sim 1.4 \times 10^{-4}$. The rejection of higher harmonics was achieved by a pair of Rh-coated mirrors at 4 mrad.

The spot size at the sample was $\sim 200 \mu\text{m} \times 250 \mu\text{m}$ ($H \times V$). The energy calibration was performed using a Cu foil. The operando XAS spectra were recorded in the fluorescence mode using a Lytle detector. The electrolysis was performed in CO₂-saturated 0.1 M KHCO₃ solution in a two-compartment H-shape cell. The sample was at 45° with respect to the incident beam direction. The electrodes were prepared as described in the “Electrochemical measurement” section. CO₂ was bubbled into the cell with a constant flow rate during the operando experiments. Kapton tape was used to seal the cell. The operando XAS spectra were measured at a potential range from 0 to -1.42 V (keeping a constant potential when recording the spectrum). The running time for each spectrum was 8 min. XAS data were analyzed using the Athena software. All the XAS spectra were normalized to unity in Athena. The FT-EXAFS spectra were calculated between 3.0 and 11.0 Å⁻¹ after weighting by k^3 .

Computational methods. All DFT calculations were performed with the Vienna Ab Initio Simulation Package (VASP) code⁵³. The Perdew–Burke–Ernzerhof was employed for electron exchange–correlation⁵⁴. Projector Augmented Wave potentials were used to describe the ionic cores⁵⁵. The atomic relaxations were carried out with the quasi-Newton minimization scheme until the maximum force on any atom was $<0.03 \text{ eV } \text{Å}^{-1}$. The geometry optimizations were performed with a plane-wave cutoff of 400 eV. Irreducible $2 \times 3 \times 1$ or $2 \times 2 \times 1$ Monkhorst Pack k -point grid was used⁵⁶, with the center shifted to the gamma point. The Fermi level was smeared with the Methfessel–Paxton approach with a smearing of 0.1 eV. Dipole corrections were included in all the calculations to minimize the inaccuracies in the total energy due to the simulated slab interactions. The dipole moment was calculated parallel to the z -direction.

The implicit solvent effect was considered by using VASPsol⁵⁷. The solvent dielectric constant was set to be 78.4, the width of dielectric cavity was 0.6 Å, the cutoff charge density was set to be 0.0025, and the effective cavity surface tension was 0.000525.

The lattice constant of Cu was optimized to be 3.64 Å in its fcc crystal structure. The Cu [101] RNPs were built based on a rectangular $5 \times 5 \times 1$ Cu (101) surface; the four triangular sidewalls of the nanopillar are (100) and (111) facets at intervals. The base layers were fixed while nanopillars and adsorbates were permitted to fully relax in all configurations. The Cu (111) surfaces was constructed with $4 \times 4 \times 4$ supercells, respectively, both with two bottom layers fixed. Two topmost layers and adsorbates were free to move in all directions. The vertical separation between periodically repeated images was set to be at least 15 Å in all cases, to ensure no interaction between images.

The free energies of adsorbed species, calculated based on the computational hydrogen electrode model⁵⁵, are defined as:

$$\Delta G_{\text{ad}} = \Delta E_{\text{ad}} + \text{ZPE} - T\Delta S \quad (1)$$

where ZPE is the zero-point energy correction and $T\Delta S$ is the entropy correction, which were computed with standard methods⁵⁸.

The formation free energy of *COH-CO ($\Delta G_{*COH-CO}$) is calculated as

$$\Delta G_{*COH-CO} = G_{\text{total}} - (G_{*CO} + G_{H_2}/2) \quad (2)$$

where G_{total} is the free energy of a surface with adsorbed *COH-CO, G_{*CO} is the free energy of a surface with two adsorbed CO molecules, and G_{H_2} is the energy of a hydrogen molecule, which is -6.83 eV.

The formation free energy of *CHO (ΔG_{*CHO}) is calculated as

$$\Delta G_{*CHO} = G_{\text{total}} - (G_{*CO} + G_{H_2}/2) \quad (3)$$

where G_{total} is the free energy of a surface with adsorbed *CHO and G_{*CO} is the free energy of a surface with one adsorbed CO molecule. The free energy of relevant gas phases are listed in Supplementary Table 6.

Limiting potential (U_{limiting}) is used to describe the lowest potential requirement to eliminate the free energy difference of the PDS, calculated as:

$$U_{\text{limiting}} = -\Delta G_{\text{max}}/e \quad (4)$$

We applied the CEP model proposed by Head-Gordon and colleagues⁴⁹ to consider the effect of applied potential on reactions. We simulated each surface with different electron numbers, i.e., $-2|e|$, $0|e|$, and $+2|e|$. We then carried out potential calculation to obtain work function of each surface and corresponding electrode potentials. The electrode potential (U) of the slab relative to the normal hydrogen electrode (NHE) can be estimated from the work function, ϕ , relative to that of the NHE (ϕ_{NHE}).

$$U = \phi - \phi_{\text{NHE}} \quad (5)$$

where $\phi_{\text{NHE}} = 4.5 \text{ V}$ as the work function of the reference system⁵⁹. The linear relationship of electrode potentials and electron numbers on different models are presented in Supplementary Fig. 26. From Supplementary Fig. 26, different numbers of electrons were assigned to corresponding surfaces to simulate the desired electrode potential as shown in Supplementary Table 7.

Data availability

The data that support the findings of this study are available from the authors upon request.

Received: 25 July 2021; Accepted: 6 November 2021;

Published online: 24 November 2021

References

- Obama, B. The irreversible momentum of clean energy. *Science* **355**, 126–129 (2017).
- Armstrong, R. C. et al. The frontiers of energy. *Nat. Energy* **1**, 15020 (2016).
- De Luna, P. et al. What would it take for renewably powered electrosynthesis to displace petrochemical processes? *Science* **364**, eaav3506 (2019).
- Bushuyev, O. S. et al. What should we make with CO₂ and how can we make it? *Joule* **2**, 825–832 (2018).
- Nitopi, S. et al. Progress and perspectives of electrochemical CO₂ reduction on copper in aqueous electrolyte. *Chem. Rev.* **119**, 7610–7672 (2019).
- Bagger, A., Ju, W., Varela, A. S., Strasser, P. & Rossmeisl, J. Electrochemical CO₂ reduction: a classification problem. *Chemphyschem* **18**, 3266–3273 (2017).
- Perez-Ramirez, J. & Lopez, N. Strategies to break linear scaling relationships. *Nat. Catal.* **2**, 971–976 (2019).
- Ross, M. B. et al. Designing materials for electrochemical carbon dioxide recycling. *Nat. Catal.* **2**, 648–658 (2019).
- Choi, C. et al. Highly active and stable stepped Cu surface for enhanced electrochemical CO₂ reduction to C₂H₄. *Nat. Catal.* **3**, 804–812 (2020).
- Kim, M. J. et al. Ethylenediamine promotes Cu nanowire growth by inhibiting oxidation of Cu(111). *J. Am. Chem. Soc.* **139**, 277–284 (2017).
- Cheng, T., Xiao, H. & Goddard, W. A. Nature of the active sites for CO reduction on copper nanoparticles; suggestions for optimizing performance. *J. Am. Chem. Soc.* **139**, 11642–11645 (2017).
- Zhong, D. et al. Coupling of Cu(100) and (110) facets promotes carbon dioxide conversion to hydrocarbons and alcohols. *Angew. Chem. Int. Ed.* **60**, 4879–4885 (2021).
- Xiong, L. et al. Breaking the linear scaling relationship by compositional and structural crafting of ternary Cu-Au/Ag nanoframes for electrocatalytic ethylene production. *Angew. Chem. Int. Ed.* **60**, 2508–2518 (2021).
- Xu, H. et al. Highly selective electrocatalytic CO₂ reduction to ethanol by metallic clusters dynamically formed from atomically dispersed copper. *Nat. Energy* **5**, 623–632 (2020).
- De Luna, P. et al. Catalyst electro-redeposition controls morphology and oxidation state for selective carbon dioxide reduction. *Nat. Catal.* **1**, 103–110 (2018).
- Favaro, M. et al. Subsurface oxide plays a critical role in CO₂ activation by Cu(111) surfaces to form chemisorbed CO₂, the first step in reduction of CO₂. *Proc. Natl Acad. Sci. USA* **114**, 6706–6711 (2017).
- Wang, X. et al. Efficient electrically powered CO₂-to-ethanol via suppression of deoxygenation. *Nat. Energy* **5**, 478–486 (2020).
- Nam, D. H. et al. Molecular enhancement of heterogeneous CO₂ reduction. *Nat. Mater.* **19**, 266–276 (2020).
- Gu, H. et al. Graphdiyne/graphene heterostructure: a universal 2D scaffold anchoring monodispersed transition-metal phthalocyanines for selective and durable CO₂ electroreduction. *J. Am. Chem. Soc.* **143**, 8679–8688 (2021).
- Wu, Y., Jiang, Z., Lu, X., Liang, Y. & Wang, H. Domino electroreduction of CO₂ to methanol on a molecular catalyst. *Nature* **575**, 639–642 (2019).
- Moller, T. et al. Electrocatalytic CO₂ reduction on CuO_x nanocubes: tracking the evolution of chemical state, geometric structure, and catalytic selectivity using operando spectroscopy. *Angew. Chem. Int. Ed.* **59**, 17974–17983 (2020).
- Jung, H. et al. Electrochemical fragmentation of Cu₂O nanoparticles enhancing selective C-C coupling from CO₂ reduction reaction. *J. Am. Chem. Soc.* **141**, 4624–4633 (2019).
- Yi, J. D. et al. Highly selective CO₂ electroreduction to CH₄ by in situ generated Cu₂O single-type sites on a conductive MOF: stabilizing key intermediates with hydrogen bonding. *Angew. Chem. Int. Ed.* **59**, 23641–23648 (2020).
- Wang, Y. R. et al. Oriented electron transmission in polyoxometalate-metalloporphyrin organic framework for highly selective electroreduction of CO₂. *Nat. Commun.* **9**, 4466 (2018).
- Mukhopadhyay, S. et al. Assembly of a metal-organic framework (MOF) membrane on a solid electrocatalyst: introducing molecular-level control over heterogeneous CO₂ reduction. *Angew. Chem. Int. Ed.* **60**, 13423–13429 (2021).
- Nam, D. H. et al. Intermediate binding control using metal-organic frameworks enhances electrochemical CO₂ reduction. *J. Am. Chem. Soc.* **142**, 21513–21521 (2020).
- Yao, D. et al. The controllable reconstruction of Bi-MOFs for electrochemical CO₂ reduction through electrolyte and potential mediation. *Angew. Chem. Int. Ed.* **60**, 18178–18184 (2021).
- Nam, D. H. et al. Metal-organic frameworks mediate Cu coordination for selective CO₂ electroreduction. *J. Am. Chem. Soc.* **140**, 11378–11386 (2018).
- Zheng, W. & Lee, L. Y. S. Metal-organic frameworks for electrocatalysis: catalyst or precatalyst? *ACS Energy Lett.* **6**, 2838–2843 (2021).
- Chen, T. et al. Continuous electrical conductivity variation in M₃(hexaiminotriphenylene)₂ (M = Co, Ni, Cu) MOF alloys. *J. Am. Chem. Soc.* **142**, 12367–12373 (2020).
- Campbell, M. G., Sheberla, D., Liu, S. F., Swager, T. M. & Dinca, M. Cu₃(hexaiminotriphenylene)₂: an electrically conductive 2D metal-organic framework for chemiresistive sensing. *Angew. Chem. Int. Ed.* **54**, 4349–4352 (2015).
- Campbell, M. G., Liu, S. F., Swager, T. M. & Dinca, M. Chemiresistive sensor arrays from conductive 2D metal-organic frameworks. *J. Am. Chem. Soc.* **137**, 13780–13783 (2015).
- Lian, Y. et al. Unpaired 3d electrons on atomically dispersed cobalt centres in coordination polymers regulate both oxygen reduction reaction (ORR) activity and selectivity for use in zinc-air batteries. *Angew. Chem. Int. Ed.* **59**, 286–294 (2020).
- Zhang, W. et al. Atypical oxygen-bearing copper boosts ethylene selectivity toward electrocatalytic CO₂ reduction. *J. Am. Chem. Soc.* **142**, 11417–11427 (2020).
- Lian, Y. et al. Carved nanoframes of cobalt-iron bimetal phosphide as a bifunctional electrocatalyst for efficient overall water splitting. *Chem. Sci.* **10**, 464–474 (2019).
- Lin, D., Liu, Y. & Cui, Y. Reviving the lithium metal anode for high-energy batteries. *Nat. Nanotechnol.* **12**, 194–206 (2017).
- Lin, D. et al. Layered reduced graphene oxide with nanoscale interlayer gaps as a stable host for lithium metal anodes. *Nat. Nanotechnol.* **11**, 626–632 (2016).
- Kim, D., Kley, C. S., Li, Y. & Yang, P. Copper nanoparticle ensembles for selective electroreduction of CO₂ to C₂-C₃ products. *Proc. Natl Acad. Sci. USA* **114**, 10560–10565 (2017).
- Bagger, A., Ju, W., Varela, A. S., Strasser, P. & Rossmeisl, J. Electrochemical CO₂ reduction: classifying Cu facets. *ACS Catal.* **9**, 7894–7899 (2019).
- Desgranges, C. & Delhommelle, J. Molecular insight into the pathway to crystallization of aluminum. *J. Am. Chem. Soc.* **129**, 7012–7013 (2007).
- Leyssale, J. M., Delhommelle, J. & Millot, C. Reorganization and growth of metastable alpha-N₂ critical nuclei into stable beta-N₂ crystals. *J. Am. Chem. Soc.* **126**, 12286–17027 (2004).
- Luo, W., Nie, X., Janik, M. J. & Asthagiri, A. Facet dependence of CO₂ reduction paths on Cu electrodes. *ACS Catal.* **6**, 219–229 (2015).
- Chen, L., Tang, C., Jiao, Y. & Qiao, S. Z. Anomalous C-C coupling on under-coordinated Cu (111): a case study of Cu nanopramids for CO₂ reduction reaction by molecular modelling. *ChemSusChem* **14**, 671–678 (2021).
- Cheng, T., Xiao, H. & Goddard, W. A. 3rd Full atomistic reaction mechanism with kinetics for CO reduction on Cu(100) from ab initio molecular dynamics free-energy calculations at 298 K. *Proc. Natl Acad. Sci. USA* **114**, 1795–1800 (2017).
- Jiang, K. et al. Effects of surface roughness on the electrochemical reduction of CO₂ over Cu. *ACS Energy Lett.* **5**, 1206–1214 (2020).
- Verdagué-Casadevall, A. et al. Probing the active surface sites for CO reduction on oxide-derived copper electrocatalysts. *J. Am. Chem. Soc.* **137**, 9808–9811 (2015).
- De Gregorio, G. L. et al. Facet-dependent selectivity of Cu catalysts in electrochemical CO₂ reduction at commercially viable current densities. *ACS Catal.* **10**, 4854–4862 (2020).
- Hori, Y., Takahashi, I., Koga, O. & Hoshi, N. Selective formation of C₂ compounds from electrochemical reduction of CO₂ at a series of copper single crystal electrodes. *J. Phys. Chem. B* **106**, 15–17 (2002).
- Garza, A. J., Bell, A. T. & Head-Gordon, M. Mechanism of CO₂ reduction at copper surfaces: pathways to C₂ products. *ACS Catal.* **8**, 1490–1499 (2018).
- Elhamid, M. H. A., Ateya, B. G., Weil, K. G. & Pickering, H. W. Calculation of the hydrogen surface coverage and rate constants of the hydrogen evolution reaction from polarization data. *J. Electrochem. Soc.* **147**, 2148–2150 (2000).
- Jerkiewicz, G. Electrochemical hydrogen adsorption and absorption. Part 1: Under-potential deposition of hydrogen. *Electrocatalysis* **1**, 179–199 (2010).
- Liu, K., Smith, W. A. & Burdyny, T. Introductory guide to assembling and operating gas diffusion electrodes for electrochemical CO₂ reduction. *ACS Energy Lett.* **4**, 639–643 (2019).
- Kresse, G. & Furthmüller, J. Efficient iterative schemes for ab initio total-energy calculations using a plane-wave basis set. *Phys. Rev. B* **54**, 11169–11186 (1996).
- Perdew, J. P., Burke, K. & Ernzerhof, M. Generalized gradient approximation made simple. *Phys. Rev. Lett.* **78**, 1396–1396 (1997).
- Kresse, G. & Joubert, D. From ultrasoft pseudopotentials to the projector augmented-wave method. *Phys. Rev. B* **59**, 1758–1775 (1999).
- Monkhorst, H. J. & Pack, J. D. Special points for Brillouin-zone integrations. *Phys. Rev. B* **13**, 5188–5192 (1976).
- Mathew, K., Sundararaman, R., Letchworth-Weaver, K., Arias, T. A. & Hennig, R. G. Implicit solvation model for density-functional study of nanocrystal surfaces and reaction pathways. *J. Chem. Phys.* **140**, 084106 (2014).
- Norskov, J. K. et al. Origin of the overpotential for oxygen reduction at a fuel-cell cathode. *J. Phys. Chem. B* **108**, 17886–17892 (2004).

59. Skulason, E. et al. Density functional theory calculations for the hydrogen evolution reaction in an electrochemical double layer on the Pt(111) electrode. *Phys. Chem. Chem. Phys.* **9**, 3241–3250 (2007).

Acknowledgements

This work is supported by National Key R&D Program of China (Grant No. 2020YFB1505703), National Natural Science Foundation of China (Nos. 22072101, 22075193, U1932211), Natural Science Foundation of Jiangsu Province (No. BK20211306), Six Talent Peaks Project in Jiangsu Province (No. TD-XCL-006), and the Priority Academic Program Development (PAPD) of Jiangsu Higher Education Institutions. This research is also supported by the Australian Research Council through these programs: FT190100636 and DP190103472. DFT computations for this research were undertaken with the assistance of supercomputing resources provided by the Phoenix HPC service at the University of Adelaide and the National Computational Infrastructure (NCI), which is supported by the Australian Government. The authors also thank for the support from the Honorary Professor Program of Jiangsu Province, National Key R&D Program of China (2020YFA0406103), and Collaborative Innovation Center of Suzhou Nano Science & Technology and Users with Excellence Program of Hefei Science Center CAS (2019HSC-UE002).

Author contributions

Y.P. conceived the idea and led the project. H.S. designed and performed the majority of the experiments and obtained most of the results, including material synthesis, characterization, and electrochemical tests. L.C. and Y.J. carried out the DFT calculations. K.F., Y.C. and J.Z. carried out XAS characterizations. Y.L. and M.H.R. took the Cs-TEM images and analyzed the data. Z.D., X.Y. and B.Y. helped to polish the paper. Z.D., L.X. and X.Z. devoted to the electrochemical data analysis. H.S., L.C., Z.D., Y. J. and Y.P. wrote the paper. All the authors have discussed the results.

Competing interests

The authors declare no competing interests.

Additional information

Supplementary information The online version contains supplementary material available at <https://doi.org/10.1038/s41467-021-27169-9>.

Correspondence and requests for materials should be addressed to Jun Zhong, Yan Jiao or Yang Peng.

Peer review information *Nature Communications* thanks Christoph Baeumer and the other anonymous reviewer(s) for their contribution to the peer review of this work. Peer reviewer reports are available.

Reprints and permission information is available at <http://www.nature.com/reprints>

Publisher's note Springer Nature remains neutral with regard to jurisdictional claims in published maps and institutional affiliations.



Open Access This article is licensed under a Creative Commons Attribution 4.0 International License, which permits use, sharing, adaptation, distribution and reproduction in any medium or format, as long as you give appropriate credit to the original author(s) and the source, provide a link to the Creative Commons license, and indicate if changes were made. The images or other third party material in this article are included in the article's Creative Commons license, unless indicated otherwise in a credit line to the material. If material is not included in the article's Creative Commons license and your intended use is not permitted by statutory regulation or exceeds the permitted use, you will need to obtain permission directly from the copyright holder. To view a copy of this license, visit <http://creativecommons.org/licenses/by/4.0/>.

© The Author(s) 2021